

# Deuteron Quadrupolar Chemical Exchange Saturation Transfer (Q-CEST) Solid-State NMR for Static Powder Samples: Approach and Applications to Amyloid- $\beta$ Fibrils

Liliya Vugmeyster,<sup>\*[a]</sup> Dmitry Ostrovsky,<sup>[b]</sup> and Riqiang Fu<sup>[c]</sup>

We provide an experimental and computational framework for  $^2\text{H}$  quadrupolar chemical exchange saturation transfer NMR experiments (Q-CEST) under static solid-state conditions for the quantification of dynamics on  $\mu\text{s}$ -ms timescales. Simulations using simple 2-site exchange models provide insights into the relation between spin dynamics and motions. Biological applications focus on two sites of amyloid- $\beta$  fibrils in the 3-fold symmetric polymorph. The first site, the methyl group of A2 of the disordered N-terminal domain, undergoes diffusive motions and conformational exchange due to transient interactions.

Earlier  $^2\text{H}$  rotating frame relaxation and quadrupolar CPMG measurements are combined with the Q-CEST approach to characterize the multiple conformational states of the domain. The second site, the methyl group of M35, spans the water-accessible cavity inside the fibrils' core and undergoes extensive rotameric exchange. Q-CEST permits us to refine the rotameric exchange model for this site and allows the more precise determination of populations and rotameric exchange rate constants than line shape analysis.

## 1. Introduction

Chemical exchange saturation transfer (CEST) experiments are widely used in solution NMR spectroscopy for the elucidation of minor conformational states exchanging with the major state at a slow timescale.<sup>[1–4]</sup> The weak RF field saturates the minor resonance when its offset matches its chemical shift and the resulting reduction in the spin polarization transferred to the major resonance via the chemical exchange. In a similar dark saturation transfer (DEST) approach,<sup>[5]</sup> the minor state, which is not visible due to a very large transverse relaxation rate, can become saturated and observed via the transfer of the saturated coherence to the major state during the conformational exchange. Simulations of these processes often involve Bloch–McConnell equations<sup>[6]</sup> and the Redfield limit approximation.<sup>[7]</sup>

The situation in solids and, especially, for quadrupolar nuclei, is more complicated due to the presence of anisotropic interactions that require, in general the full Liouvillian treatment.<sup>[8–9]</sup> An interesting application has been discussed by Siemer et al.<sup>[10]</sup> CEST measurements can, in essence, be considered to be an off-resonance longitudinal rotating frame  $R_{1\rho}$

experiment. Figure 1 shows an example of the pulse sequence used in this work, in which a saturation period is followed by the quadrupolar echo detection scheme.<sup>[11]</sup> The evolution of such conditions in the absence of exchange has been considered in detail.<sup>[12–14]</sup> It is useful to extend the experimental and simulations approaches of CEST to deuterium nuclei, which are sensitive to motions.<sup>[11]</sup> Deuterium has a modest quadrupolar coupling constant, with a typical upper limit of about 200 kHz, which makes it easy to work with experimentally. Further, the interaction is large enough to render most chemical shift anisotropy and dipolar interactions negligible, which simplifies theoretical and computational treatments.<sup>[15]</sup>

The goal of this work is to demonstrate how CEST can be used for applications involving deuterium nuclei under static solid-state powder conditions. The theory and computational framework within the full Liouvillian treatment is presented for the quadrupolar-CEST (Q-CEST) for deuterium nuclei and is complemented by modeled 2-site exchange examples to gain insights into the spin dynamics at the  $\mu\text{s}$ -ms timescale. We then focus on applications to biological solids, particularly to the

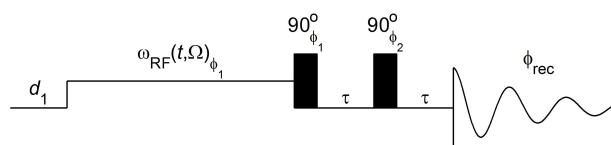


**Figure 1.** Pulse sequence for the Q-CEST experiment for  $^2\text{H}$  nuclei under static powder conditions. After the inter-scan delay  $d_1$ , the small amplitude RF saturation pulse  $\omega_{\text{RF}}(t, \Omega)$  is followed by the quadrupolar echo detection scheme  $90^\circ\text{--}\tau\text{--}90^\circ\text{--}\tau$ . The RF field strength and saturation pulse duration  $t$  are chosen to fit the dynamic profile of the system as well as its longitudinal relaxation characteristics and is applied for multiple values of the off-resonance offset  $\Omega$ . The phase cycle is  $\varphi_1 = x, -y, -x, y, x, -y, -x, y$ ;  $\varphi_2 = -y, -x, y, x, y, -y, -x, y$ ;  $\varphi_{\text{rec}} = -y, -x, y, x, -y, -x, y, x$ .

[a] Prof. L. Vugmeyster  
Department of Chemistry  
University of Colorado Denver  
Denver CO 80204, USA  
E-mail: liliya.vugmeyster@ucdenver.edu

[b] Dr. D. Ostrovsky  
Department of Mathematics  
University of Colorado Denver  
Denver CO 80204, USA

[c] Dr. R. Fu  
National High Field Magnetic Laboratory  
Tallahassee, FL 32310, USA

Supporting information for this article is available on the WWW under <https://doi.org/10.1002/cphc.201901053>

amyloid- $\beta$  ( $A\beta_{1-40}$ ) fibrils labeled with deuterium at two sites. One of these sites, the methyl group of A2, belongs to the flexible N-terminal domain (Figure 2A), the dynamics of which we have previously studied with on-resonance  $R_{1\rho}$  relaxation, quadrupolar Carr-Purcell-Meiboom-Gill (QCPMG) and line shape approaches.<sup>[16–17]</sup> The second site, the methyl group of the M35 side chain, is a part of the water-accessible cavity of the fibrils<sup>[18–21]</sup> (Figure 2A–C) and has been previously studied by line shape analysis and longitudinal relaxation.<sup>[21–22]</sup> In both these cases, Q-CEST provides additional information on the dynamics that complements previous measurements.

## 2. Results and Discussion

### 2.1. Theory Overview

The density matrix for the spin-1 system can be written on the basis of the following operators:<sup>[13]</sup>

$$\begin{aligned}\widehat{S}_x &= \frac{1}{2} \begin{pmatrix} 0 & 1 & 0 \\ 1 & 0 & 1 \\ 0 & 1 & 0 \end{pmatrix}, \widehat{S}_y = \frac{1}{2} \begin{pmatrix} 0 & -i & 0 \\ i & 0 & -i \\ 0 & i & 0 \end{pmatrix}, \\ \widehat{J}_x &= \frac{1}{2} \begin{pmatrix} 0 & -i & 0 \\ i & 0 & i \\ 0 & -i & 0 \end{pmatrix}, \widehat{J}_y = \frac{1}{2} \begin{pmatrix} 0 & 1 & 0 \\ 1 & 0 & -1 \\ 0 & -1 & 0 \end{pmatrix} \\ \widehat{S}_z &= \frac{1}{\sqrt{2}} \begin{pmatrix} 1 & 0 & 0 \\ 0 & 0 & 0 \\ 0 & 0 & -1 \end{pmatrix}, \widehat{J}_z = \frac{1}{\sqrt{2}} \begin{pmatrix} 0 & 0 & -i \\ 0 & 0 & 0 \\ i & 0 & 0 \end{pmatrix}, \\ \widehat{Q} &= \frac{1}{\sqrt{6}} \begin{pmatrix} 1 & 0 & 0 \\ 0 & -2 & 0 \\ 0 & 0 & 1 \end{pmatrix}, \widehat{K} = \frac{1}{\sqrt{2}} \begin{pmatrix} 0 & 0 & 1 \\ 0 & 0 & 0 \\ 1 & 0 & 0 \end{pmatrix}.\end{aligned}\quad (1)$$

$\widehat{S}_x$ ,  $\widehat{S}_y$ ,  $\widehat{J}_x$ , and  $\widehat{J}_y$  are coherences associated with the single-quantum transitions,  $\widehat{K}$  and  $\widehat{J}_z$  are coherences associated with the double-quantum transitions, and  $\widehat{S}_z$  and  $\widehat{Q}$  represent Zeeman and quadrupolar order. The ninth coherence is proportional to the unity operator and does not participate in any interactions. The operators in the basis of Eq. (1) obey the following normalization condition,  $\text{tr}(O_k^+ O_l) = \delta_{kl}$ .

During the saturation period and in the frame rotating with the Larmor frequency, the Hamiltonian is given by Eq. (2):

$$\widehat{H} = \sqrt{\frac{2}{3}} \omega_Q \widehat{Q} + \sqrt{2} \omega_{RF} (\widehat{S}_x \cos \Omega t + \widehat{S}_y \sin \Omega t), \quad (2)$$

where  $\omega_{RF}$  is the RF field strength and  $\Omega$  is its off-resonance offset.

$$\omega_Q = \frac{3\pi}{2} C_q \left( \frac{3\cos^2\theta - 1}{2} + \frac{\eta}{2} \sin^2\theta \cos 2\phi \right) \quad (3)$$

is the frequency of the secular part of the quadrupole interaction, with the angles  $(\theta, \phi)$  representing the rotation of the principal-axis system of the quadrupole interaction with respect to the laboratory frame. The quadrupolar coupling

constant is given by  $C_q = \frac{e^2 q Q}{h}$ , and  $\eta = \frac{q_{xx} - q_{yy}}{q_{zz}}$  represents the asymmetry of the tensor, defined in the interval  $0 \leq \eta \leq 1$  with  $|q_{zz}| \geq |q_{yy}| \geq |q_{xx}|$ .  $eQ$  is the electric quadrupole moment of the nucleus and  $eq$  is the largest component of the electric field gradient.

In the presence of molecular motions, the value of  $\omega_Q$  for an individual crystallite does not remain constant, but rather changes due to alterations in the principal-axis system orientation. In addition to the dependence of  $\omega_Q$  originating from molecular motions, there is an additional dependence of  $\omega_Q$  in powder solids on the orientation of the crystallite to the static magnetic field, as is the case for all anisotropic interactions. Additional terms in the Hamiltonian include

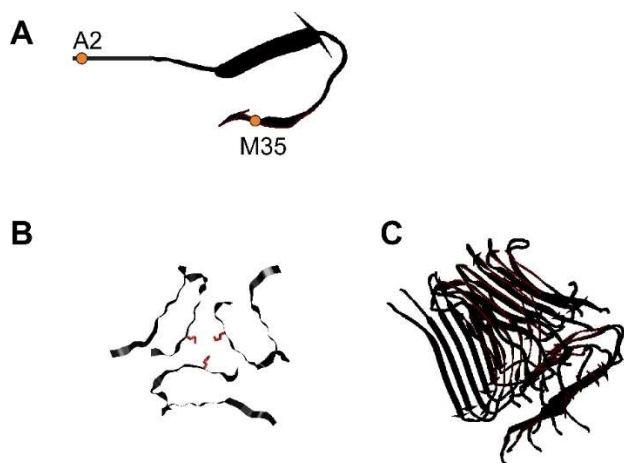


**Figure 2.** A) A diagram of one molecule of  $A\beta_{1-40}$  within the fibrillar structure. The structure of the monomer for residues 9 and beyond is taken from the protein data bank file 2LMP.pdb<sup>[34]</sup> and is shown as a ribbon diagram, while the residues 1–9 of the N-terminal domain are shown schematically as a line. The whole disordered N-terminal domain spans residues 1–16. The methyl groups of A2-CD<sub>3</sub> and M35-CD<sub>3</sub> studied in this work (orange dots) belong to the disordered N-terminal domain and the structured core, respectively. B) Top view of the 3-fold symmetric fibril structure,<sup>[34]</sup> with the side chains of M35 pointing into the water-accessible cavity shown in red. C) The ensemble of eight structural subunits of the 3-fold symmetric structure,<sup>[34]</sup> shown as black ribbon diagram made in swisspdb viewer software.<sup>[43]</sup>

quadrupole interaction terms, which fluctuate with single and double Larmor frequencies. They are treated separately through the Redfield theory.

In the frame additionally rotating around the z-axis with the offset frequency  $\Omega$ , the secular part of the Hamiltonian becomes

$$\hat{H}_{sec} = \sqrt{\frac{2}{3}}\omega_Q\hat{Q} + \sqrt{2}\omega_{RF}\hat{S}_x + \sqrt{2}\Omega\hat{S}_z \quad (4)$$

The evolution of the density matrix can be written on the basis of Eq. (1) in the superoperator formalism. The Liouville–von Neumann formalism combines the Hamiltonian superoperator for the spin density matrix with the Markovian jumps between states, with the different values of  $\omega_Q$  simulating the various spin environments. It, therefore, includes the relaxation due to the fluctuations in the  $\omega_Q$  value, which, in general, cannot be treated within the Redfield approximation. The rapidly oscillating part of the non-secular Hamiltonian, not shown explicitly in Eq. (4), is treated in the second order of the perturbation theory (i.e. the Redfield approximation for rapidly oscillating terms).<sup>[7]</sup> As we elaborate later, these include all the spectral density terms of the spectral density function of the order of the Larmor and twice the Larmor frequency.

If molecular motions are given by the discrete jumps between  $n$  sites, with the different values of  $\omega_Q$  sampled by the conformational exchange, the evolution matrix becomes

$$\frac{d}{dt} \begin{pmatrix} \rho_1 \\ \rho_2 \\ \vdots \\ \rho_n \end{pmatrix} = \begin{pmatrix} A_1 + K_{11} & K_{12} & \cdots & K_{1n} \\ K_{21} & A_2 + K_{22} & \cdots & K_{2n} \\ \vdots & \vdots & \ddots & \vdots \\ K_{n1} & K_{n2} & \cdots & A_n + K_{nn} \end{pmatrix} \begin{pmatrix} \rho_1 \\ \rho_2 \\ \vdots \\ \rho_n \end{pmatrix} \quad (5)$$

where  $\rho_i = (S_x, S_y, J_x, J_y, J_z, K, S_z, Q)^T$  are the components of the density matrix for site  $i$  on the basis of the operators of Eq. (1), with the coefficients corresponding to the components of the density matrix as for the operators themselves, but without hats. The off-diagonal blocks represent conformational exchange and are given by  $K_{ij} = k_{ij}I$ , where  $I$  is the  $8 \times 8$  identity matrix and the diagonal blocks  $K_{ii} = -\sum_{j \neq i} K_{ji}$  provide the conservation of probability. The  $8 \times 8$  evolution  $A_i$  matrices, which include the coherent evolution given by  $\hat{H}_{sec}$  as well as relaxation in the Redfield limit due to the rapidly oscillating non-secular components, are given by

$$A = \begin{pmatrix} -r_1 & -\Omega & -\omega_Q & 0 & 0 & 0 & 0 & 0 \\ \Omega & -r_1 & 0 & \omega_Q & 0 & 0 & -\omega_{RF} & 0 \\ \omega_Q & 0 & -r_2 & \Omega & 0 & -\omega_{RF} & 0 & -\sqrt{3}\omega_{RF} \\ 0 & -\omega_Q & -\Omega & -r_2 & \omega_{RF} & 0 & 0 & 0 \\ 0 & 0 & 0 & -\omega_{RF} & -r_3 & 2\Omega & 0 & 0 \\ 0 & 0 & \omega_{RF} & 0 & -2\Omega & -r_3 & 0 & 0 \\ 0 & \omega_{RF} & 0 & 0 & 0 & 0 & -r_4 & 0 \\ 0 & 0 & \sqrt{3}\omega_{RF} & 0 & 0 & 0 & 0 & -r_5 \end{pmatrix} \quad (6)$$

The diagonal terms represent relaxation due to rapidly oscillating quadrupole interaction terms similar to the approach of van der Maarel.<sup>[23]</sup> In particular, these terms are treated as a perturbation to the Hamiltonian of Eq. (4) and their secular contribution can be calculated in the second order of the perturbation theory:

$$r_1 = \frac{5}{2}J_1(\omega_L) + J_2(2\omega_L)$$

$$r_2 = \frac{1}{2}J_1(\omega_L) + J_2(2\omega_L)$$

$$r_3 = J_1(\omega_L) + J_2(2\omega_L)$$

$$r_4 = J_1(\omega_L) + 4J_2(2\omega_L)$$

$$r_5 = 3J_1(\omega_L)$$

The relaxation terms in van der Maarel<sup>[23]</sup> also include relaxation due to changes in  $\omega_Q$ , which are calculated using the Liouville – von Neumann formalism in this work and therefore are excluded from Eq. (6). The  $J_1$  and  $J_2$  terms are treated within the Redfield approximation based on the assumption that the relaxation rate is significantly smaller than the rate of the motions that cause it.<sup>[7]</sup> Indeed, the order-of-magnitude estimate of the relaxation rates due to the exchange involving different Zeeman levels is  $\frac{\omega_Q^2 k}{\omega_L^2 + k^2} < \left(\frac{\omega_Q}{\omega_L}\right)^2 k \ll k$ , where  $k$  is a typical motional rate constant, while for relaxation rates due to fluctuations originating from the secular terms at frequencies much smaller than Larmor frequency the relaxation is proportional to  $\frac{\omega_Q^2}{k}$  and can be on the order of  $k$  or even smaller, depending on the relationship between  $k$  and  $\omega_Q$ .

## 2.2. Examples of Q-CEST Profiles for Different 2-Site Exchange Scenarios

Conformational exchange can modulate an anisotropic interaction by affecting either the intrinsic tensor parameters of the exchanging sites (i.e. modifying the spin part of the interaction)

or by effecting the spatial part of the interaction via the change in orientation. Both cases lead to a modulation of the value of  $\omega_Q$  (Eq. (3)) entering into the evolution matrix of Eq. (6).

We consider several simple cases (Figure 3 and Figure S1 in the Supporting Information) for both these qualitatively similar scenarios. Figure 3 shows a 2-site exchange between sites with two values of  $C_{qj}$ , namely 180 and 55 kHz, which are taken as typical cases of the  $^2\text{H}$  tensor in the presence and absence of methyl fast rotations.<sup>[15]</sup> The populations are taken in the 1:9 ratio. The plots are shown for the ratios of intensities, at times  $t$  and  $t=0$ , referred to as  $I(t)/I(0)$ . The intensities are integrated over the entire spectra. For the range of values of the conformational exchange rate constants  $k_{\text{ex}}$ , the saturation profiles are very sensitive to the actual rate:  $1 \cdot 10^3$  to  $1 \cdot 10^6 \text{ s}^{-1}$  for the case of Figure 3 and in some cases  $1 \cdot 10^2$  to  $1 \cdot 10^8 \text{ s}^{-1}$  for the additional examples shown in Figure S1. Outside this range  $I(t)/I(0) = 1$  for all offsets but zero, for which the  $I_z$  component is not locked and undergoes oscillations. The effective spin-locking of the  $I_z$  component by small RF fields is possible, as it commutes with the secular part of the quadrupolar operator. A possible treatment of the saturation profiles could be scanning  $I(t)/I(0)$  over the values that coincide with the off-resonance frequency  $\Omega/2\pi$ . However, in general, significant spectral distortions not only occur at frequencies in the immediate proximity of  $\Omega/2\pi$ , an example of which is demonstrated in Figure S2 for the parameters of Figure 3. Thus, a more general

approach would be to choose either the entire powder pattern or the region of the maximum spectral distortion to analyze the saturation profiles  $I(t)/I(0)$ . This approach also emphasizes the strength of the CEST technique in terms of local irradiation affecting the broad powder pattern.

To gain some physical insights, it is also instructive to examine the saturation profiles of individual crystallites. Figure 4 provides such examples for the absence and presence of motions. The evolution of the  $I_z$  component due to the coherent interactions under spin-locking conditions has been considered for quadrupolar nuclei by Vega<sup>[12-13]</sup> and Wimperis and co-workers.<sup>[14,24]</sup> In the absence of exchange,  $I_z$  coherence undergoes oscillations, which are especially noticeable near the condition  $\Omega = \pm\omega_Q$ . The blue line in Figure 4 corresponds to the maximum of these oscillations. The width of this resonance is dependent on the value of  $\omega_{\text{RF}}$  (Figure S3). Motions significantly broaden these profiles when  $k_{\text{ex}}$  is in the middle of the sensitivity range. Figure 5 shows a detailed example of how different values of  $k_{\text{ex}}$  affect such broadening for one crystallite orientation. For a  $k_{\text{ex}}$  of  $1 \cdot 10^3 \text{ s}^{-1}$ , the profiles are effectively in the static regime with two subsets of sites giving rise to the two singularities corresponding to the individual  $\omega_q$  values in each of the conformers. As the rate constant increases toward the sensitivity range, a typical broadening (coalescence) is observed similar to that seen for conformational exchange in solution NMR in the presence of two values of isotropic chemical shifts

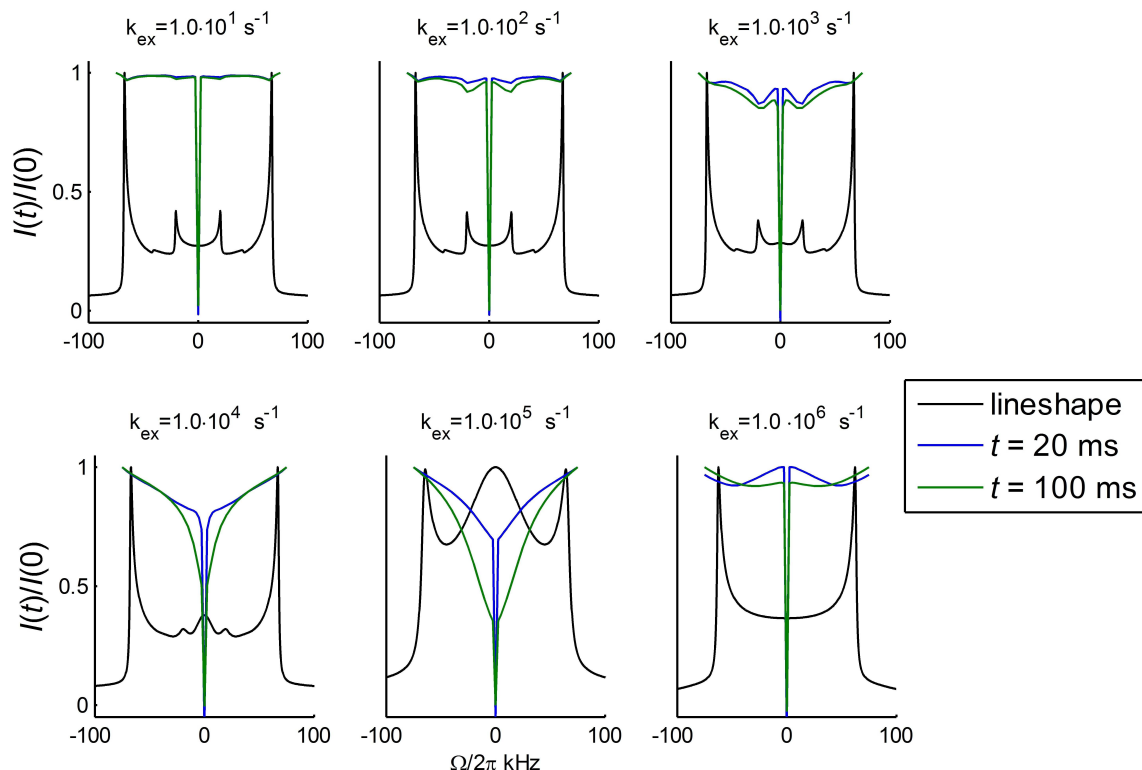


**Figure 3.** Simulated Q-CEST profiles for the 2-site exchange model with  $C_{q,1} = 55 \text{ kHz}$ ,  $C_{q,2} = 180 \text{ kHz}$ ,  $\eta_1 = \eta_2 = 0$ ,  $p_1 = 10\%$  and different values of  $k_{\text{ex}}$  indicated on the panels. Powder-averaged values of  $I(t)/I(0)$  versus off-resonance offset  $\Omega/2\pi$  for saturation times of 20 ms (green line) and 100 ms (blue line) and  $\omega_{\text{RF}}/2\pi = 2 \text{ kHz}$ . The black lines show the corresponding quadrupolar echo line shapes, where the  $x$ -axis stands for spectral frequency. 4,000 crystallite orientations were used to represent a static powder solid. Homogeneous contributions to the linewidth are not included in the simulations as well as longitudinal relaxation effects.

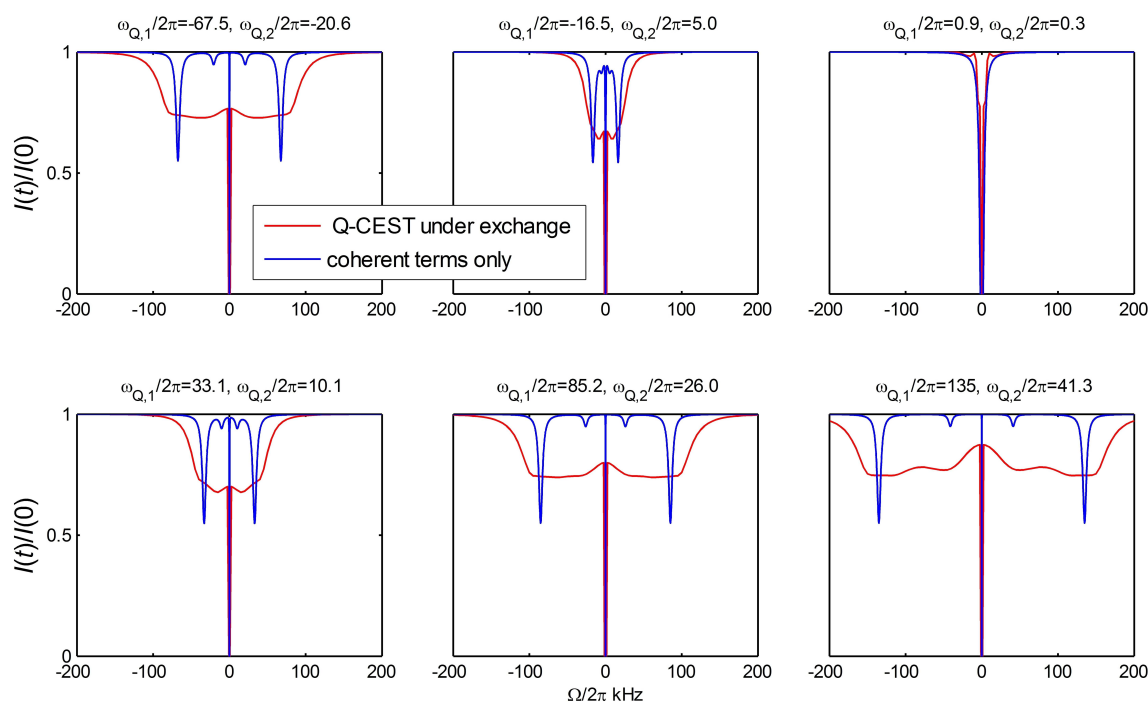


**Figure 4.** Examples of the Q-CEST profiles of  $I(t)/I(0)$  versus  $\Omega/2\pi$  for the individual crystallites (red lines) of the 2-site exchange model  $C_{q,1} = 55$  kHz,  $C_{q,2} = 180$  kHz,  $\eta_1 = \eta_2 = 0$ ,  $p_1 = 10\%$  and  $k_{ex} = 1 \cdot 10^5$  s $^{-1}$ . The values of  $\omega_{Q,1}/2\pi$  and  $\omega_{Q,2}/2\pi$  are indicated directly on the panels in units of kHz.  $\omega_{RF}/2\pi = 2$  kHz and saturation time  $t = 100$  ms. The blue lines represent the corresponding amplitudes of coherent evolution given by the minimum value of  $I(t)/I(0)$  over the oscillation period.

in the two exchanging sites.<sup>[25]</sup> When  $k_{ex}$  further increases to about  $1 \cdot 10^7$  s $^{-1}$ , the dynamics converge to the line narrowing case, with the minimum observed at the weighted average position of  $\omega_Q$  for the two exchanging sites. In this fast regime, relaxation is ineffective and coherent oscillations can still be observed at the chosen time of 100 ms. In protein methyl groups typical relaxation times are often faster than 100 ms which imposes limitations on the experimentally relevant cest relaxation period.

To observe this broadening effect experimentally, we used dimethyl-sulfone-d<sub>6</sub> (DMS), a model compound often employed as a convenient model system for the development of solid-state NMR methodologies, particularly deuterium-based methods.<sup>[26–30]</sup> Methyl groups undergo a 2-site exchange corresponding to a 180° flip around the molecule  $C_2$  axis (Figure 6A). This in turn corresponds to a 106° angle change in the orientation for individual deuterons and fast methyl 3-site jumps. Experimental data (Figure 6B) were obtained using the pulse sequence of Figure 1 at two temperatures: 68 °C at which the flips are active and 10 °C at which the flips are frozen out; we also used a saturation field of 1.3 kHz with a saturation time of 20 ms. In both cases, the timescales of the flips are significantly slower than the value of  $C_q = 166.4$  kHz. Thus, the flip motions have a negligible effect on the line shapes<sup>[26]</sup> and the spectra represent a nearly rigid pattern narrowed by a factor of one-third due to the fast methyl rotation. The saturation profiles  $I(t)/I(0)$  in this case were obtained at the major singularities (horns) of the powder patterns in order to

compare with theoretical simulations for single crystallites of Figures 4–5. In the absence of motions of the order of  $C_q$ , the major contributions at these positions originate from crystallites at a 90° angle of the largest component of the effective quadrupolar tensor with respect to the magnetic field. At 10 °C, we observe the expected dips at the horn positions corresponding to the absence of slow motions for these crystallites. The origins of the observed dips in the saturation profiles at the horns positions are due to expected resonances at the condition  $\Omega = \pm\omega_Q$ , as detailed above. At the elevated temperature, the pattern is significantly broadened and the profile deepens, again in accordance with the theoretical expectations of Figure 5. The pattern can be fitted with a flip rate of 5000 s $^{-1}$  at 68 °C, which is in agreement with the prediction based on the Arrhenius behavior obtained from other methods, particularly from the static  $^2\text{H}$   $R_{1\rho}$  measurements.<sup>[31]</sup>

Figure 3 and Figure S1 also underline the comparative range of the sensitivity of timescales for Q-CEST as opposed to the quadrupolar echo line shape experiment. One can compare the timescale ranges in which the saturation profiles are sensitive to the motional parameters: Q-CEST adds at least two orders of magnitude to the sensitivity range. There are cases of small angle jumps (Figure S1E, F) for which the line shapes are not sensitive at all to the presence of motions, while there are noticeable changes in the Q-CEST profiles. For the example considered here, the on-resonance  $R_{1\rho}$  relaxation (see the simulations in Figure S4) is also sensitive to the timescales of motions across a wide range of  $k_{ex}$  between  $1 \cdot 10^3$  and

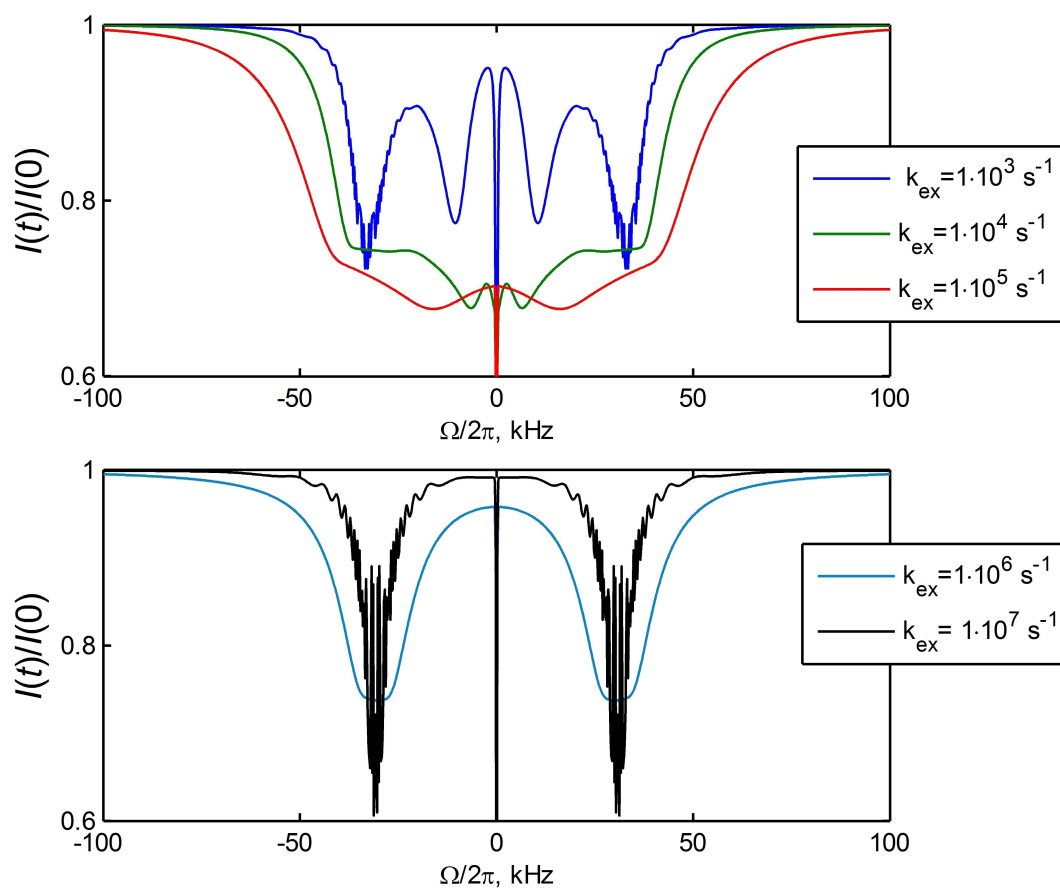


**Figure 5.** The effect of  $k_{\text{ex}}$  on the Q-CEST profiles.  $I(t)/I(0)$  versus  $\Omega/2\pi$  for the 2-site exchange model with  $C_{q,1} = 55$  kHz,  $C_{q,2} = 180$  kHz,  $\eta_1 = \eta_2 = 0$ ,  $p_1 = 10\%$  and different values of  $k_{\text{ex}}$  for a chosen crystallite orientation with  $\omega_{Q,1}/2\pi = 33.1$  kHz and  $\omega_{Q,2}/2\pi = 10.1$  kHz.  $\omega_{\text{RF}}/2\pi = 2$  kHz and saturation time  $t = 100$  ms.

$1 \cdot 10^9 \text{ s}^{-1}$ . However, these experiments would be more demanding for biological samples requiring much higher RF powers in the range of 15 to 50 kHz. Unlike the case of solution NMR in which the CEST profiles are dominated by changes in the isotropic chemical shift during the exchange process and relaxation occurs in the Redfield limit, no direct quantitative comparison can be made between the Q-CEST profiles and off-resonance transverse  $R_{1\rho}$  rates<sup>[1,4]</sup> due to the anisotropic nature of the interaction as well as the need to use much larger offsets for which the spin-locking of the transverse coherences fails. There is some similarity between the Q-CEST saturation profiles and DEST profiles.<sup>[5]</sup> However, the origins of the profiles differ, namely the DEST experiment relies on the large difference in the transverse relaxation times between the exchanging sites.

### 2.3. Experimental and Modeling Results for the Amyloid Fibril Samples

In this section, we consider applications to biological solids, particularly to the A $\beta$  fibrils implicated in Alzheimer's disease.<sup>[32–33]</sup> The fibrils were prepared using the A $\beta_{1-40}$  peptide and protocols, leading to the formation of one of the more toxic 3-fold symmetric polymorphs.<sup>[32–33]</sup> The structure of these

fibrils is available starting with residue number 9 and the rest of the flexible disordered N-terminal domain (residues 1–16) was not assigned due to extensive dynamics.<sup>[34]</sup> The core is spanned by three symmetrical A $\beta$  units (Figure 2B), with the existence of the water-accessible cavity along the fibril axis.<sup>[18–21]</sup> In particular, Wang et al.<sup>[18]</sup> delineated water cavities and interfaces in the fibrils. This application section focuses on two sites: A2 located at the beginning of the flexible N-terminus and M35 belonging to the core region but whose side chain points directly into the water-accessible cavity (Figure 2). The fibrils are in a hydrated powder state, with preparation details outlined in the Experimental Section. The two samples were prepared with a label on either of the sites, which permits us to use static  $^2\text{H}$  NMR techniques in a site-specific fashion.

Using the pulse sequence in Figure 1 and saturation fields of 1.3 and 2.5 kHz, we obtained saturation profiles at 37 °C and a 14.1 T field strength over the range of offsets from  $-50$  to  $+50$  kHz. This simple one-dimensional pulse sequence consists of a weak amplitude saturation field followed by the detection period, which for the case of deuterium is best performed via the quadrupolar echo detection scheme.<sup>[35]</sup> Frequencies closer to the middle of the spectra were sampled with a smaller step size to better define the profiles. The chosen saturation times were between 1 and 40 ms. The time of about 20 ms was in a

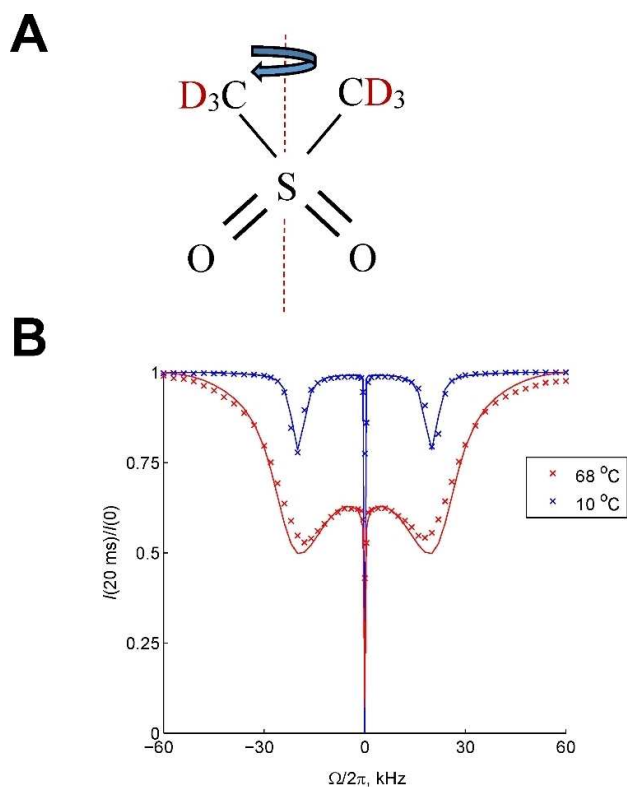


**Figure 6.** A) The structure of DMS highlighting the  $180^\circ$  flipping motion around the C2 axis. B) Experimental (crosses) and simulated (lines) Q-CEST profiles.  $I(t)/I(0)$  at the major singularities (horns) positions of the powder pattern versus  $\Omega/2\pi$  for saturation time  $t=20$  ms and  $\omega_{RF}/2\pi=1.3$  kHz. The data were obtained at  $68^\circ\text{C}$  (red) and  $10^\circ\text{C}$  (blue) and at 9.4 T using the pulse sequence of Figure 1 with the following parameters:  $d_1=0.4$  s,  $t=36.5$   $\mu\text{s}$  and number of scans = 128. Simulations (lines) were performed with the flip rates of 5000 and  $10$   $\text{s}^{-1}$ , and the 3-site jump rates of  $4.9 \cdot 10^9$  and  $1.1 \cdot 10^9$   $\text{s}^{-1}$  for  $68$  and  $10^\circ\text{C}$ , respectively.  $C_q$  of 166.4 kHz and 1500 tiles were employed.

range sufficient to obtain significant saturation, yet short enough to prevent sample heating. Relaxation delays were set at 0.7–1.5 seconds to further circumvent sample heating and dehydration. The longitudinal  $T_1$  relaxation times at  $37^\circ\text{C}$  were around 50 ms for the A2- $\text{CD}_3$  site and 0.3 s for the M35- $\text{CD}_3$  site.<sup>[17,22]</sup>

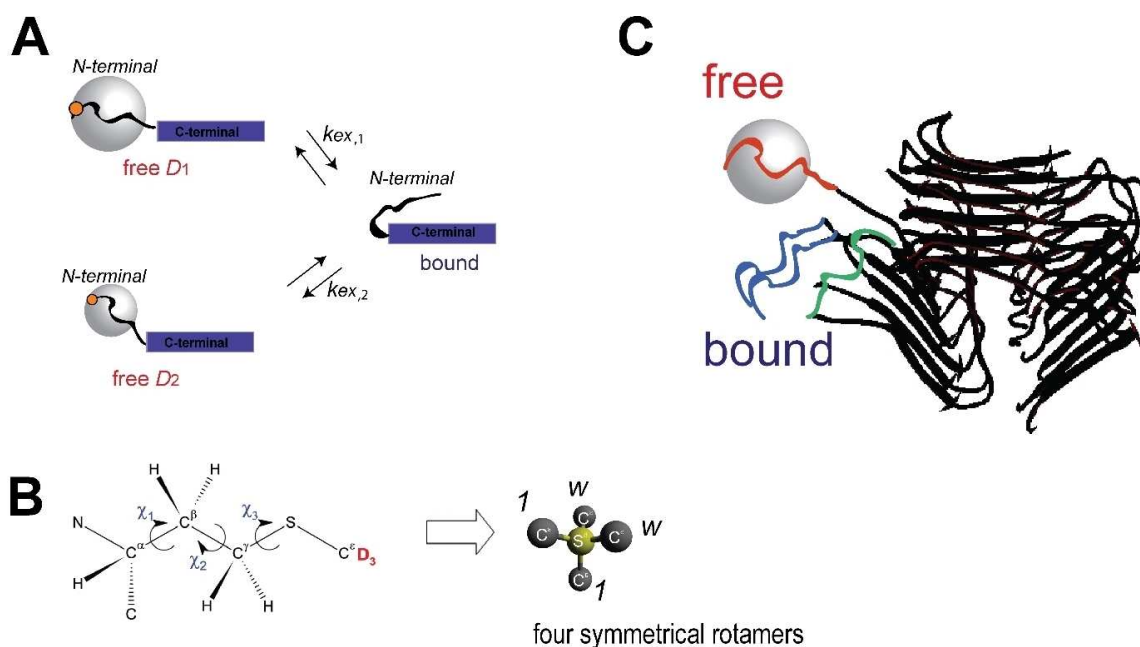
### 2.3.1. A2- $\text{CD}_3$ Sites Belonging to the Flexible N-Terminal Domain of the Amyloid Fibrils

The previous  $^2\text{H}$  line shape,  $R_{1\rho}$  relaxation and QCPMG measurements indicated that the slow timescale dynamics at the A2- $\text{CD}_3$  site are dominated by the overall motion of the disordered domain.<sup>[16–17]</sup> Two main modes (Figure 7A) define the dynamics: the domain undergoes an overall diffusive motion that can be approximated by isotropic diffusion and it also participates in the conformational exchange with the bound state, arising likely due to the transient interactions with the structured core or other intra-molecular interactions (Figure 7C). Isotropic diffusion leads to a significant narrowing of the quadrupolar

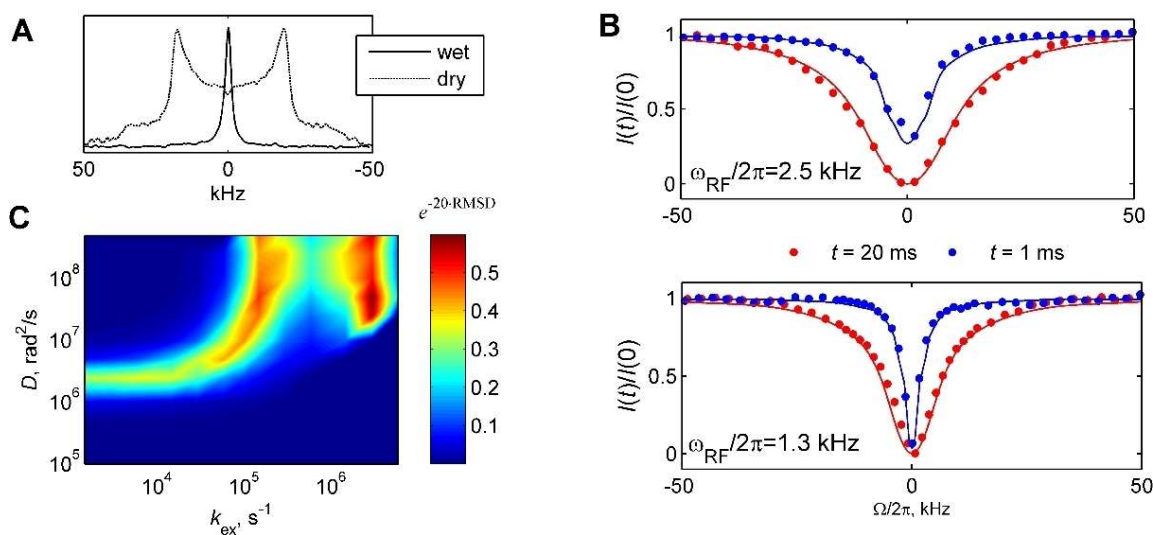
echo line shapes upon sample hydration (Figure 8A) and the presence of conformational exchange was detected via the  $^2\text{H}$  static  $R_{1\rho}$  and QCPMG measurements. The combined analysis of these data suggested that the domain actually samples two free states, with diffusion coefficients of  $1 \cdot 10^8$  and  $3 \cdot 10^6$   $\text{rad}^2/\text{s}$  at the A2 sites. Both these states exchange with the bound state but with different  $k_{\text{ex}}$  constants:  $3 \cdot 10^4$   $\text{s}^{-1}$  for the slower diffusion free state and  $3 \cdot 10^5$   $\text{s}^{-1}$  for the faster diffusion free state. Interestingly, the  $R_{1\rho}$  and QCPMG measurements are differentially sensitive to these two exchange processes:  $R_{1\rho}$  measurements probe primarily the exchange for the slow diffusion free state (with  $D=3 \cdot 10^6$   $\text{rad}^2/\text{s}$ ), while the QCPMG experiment primarily probes the exchange process of the fast diffusion state (with  $D=1 \cdot 10^8$   $\text{rad}^2/\text{s}$ ). The relative populations of the slow and fast diffusion states are 25% and 75%, respectively and the relative fraction of the bound state to the two free states is 8%.

Figure 8B shows the experimental and simulated profiles of  $I(t)/I(0)$  for the two field strengths of  $\omega_{RF}/2\pi=1.3$  and  $\omega_{RF}/2\pi=2.5$  kHz and the saturation times of  $t=1$  and  $t=20$  ms. The intensities are integrated over the entire spectrum and no spectral distortions are visible from the quadrupolar echo line shape in Figure 8A; only the overall change in intensity is modified upon scanning over the values of the offsets. The simulations according to the model in Figure 7A using the parameters obtained previously from the  $R_{1\rho}$  and QCPMG measurements reproduce the profiles rather well for all the values of  $\omega_{RF}/2\pi$  and  $t$ . The diffusion mode alone cannot match the entire profile (Figure S5A): while the central region from about  $-12$  to  $12$  kHz can be matched by the diffusion mode, the wide component of the profile requires an additional modulation. Conformational exchange with the rigid bound state (in which the quadrupolar interaction is not affected by the diffusion) provides this additional modulation with the strong influence on the sides of the profiles (Figure S5B).

We then explore the sensitivity of the fits to the model parameters for a simpler model involving a single free state undergoing isotropic diffusion with the coefficient  $D$  and exchanging with the bound state (still with a population proportion of 8%) with the rate constant  $k_{\text{ex}}$ . We focus on the experimental  $I(t)/I(0)$  profile for  $\omega_{RF}/2\pi=1.3$  kHz, where  $t=20$  ms, and create a three-dimensional RMSD heat map plot between the experimental and simulated data as a function of  $D$  and  $k_{\text{ex}}$  (Figure 8C). The plot of  $\exp(-20 \cdot \text{RMSD})$ , chosen to highlight the regions of the best fit, indicates two maxima, namely one sharp peak at  $D=5 \cdot 10^7$   $\text{rad}^2/\text{s}$  and  $k_{\text{ex}}=3 \cdot 10^6$   $\text{s}^{-1}$ , which is outside the range of  $k_{\text{ex}}$  values detected by the  $R_{1\rho}$  and QCPMG measurements, and the whole subset of  $D$  and  $k_{\text{ex}}$  values falling on a ridge consistent with the values spanned by the continuum of the two states detected by the  $R_{1\rho}$  and QCPMG measurements. Thus, the combined analysis of all three types of measurements geared toward the detection of conformational exchange processes suggests that the dynamical ensemble of the N-terminal domain of  $\text{A}\beta_{1-40}$  fibrils spans multiple free states with somewhat different values of the diffusion coefficients and all exchange with the single bound state.



**Figure 7.** A) Motional model for the motions of the A2-CD<sub>3</sub> site (orange dot), dominated by the overall motion of the N-terminal domain based on previous work.<sup>[16–17]</sup> The N-terminal domain (curved line) transiently interacts with the structured C-terminal domain (blue rectangle). In the two free states, the N-terminal domain is assumed to undergo isotropic diffusion with the diffusion coefficients  $D_1$  and  $D_2$ ,  $D_1 \gg D_2$ , represented by the gray spheres, while in the bound state, intra- or inter-molecular interactions quench this mode. The timescales of the interactions are given by the two chemical exchange rate constants,  $k_{ex,1}$  and  $k_{ex,2}$ . B) The motional model for the M35-CD<sub>3</sub> site, with the side chain  $\chi_1$ ,  $\chi_2$  and  $\chi_3$  dihedral angles indicated by the curved arrows and position of the deuterium label at the methyl group shown in red based on previous work.<sup>[22]</sup> Four artificial symmetrical conformers pointing to the corners of a tetrahedron from the sulfur atom. Line shapes can be fitted with one major and three minor conformers in a  $w:1:1:1$  ratio undergoing conformational exchange with an identical jump rate for all conformers. The Q-CEST results point to two major and two minor conformers in a  $w:w:1:1$  population ratio. An additional mode of fast methyl 3-site jumps is included in the effective value of the quadrupolar coupling constant, corresponding to  $C_q$  of 55.5 and 58 kHz for A2 and M35, respectively. C) Schematic representation of free (orange wiggly line) and bound (blue and green wiggly lines) states of N-terminal subdomain with the 3-fold wild-type fibrils structure. The 3-fold symmetric fibril core is taken from 2LMP.pdb file<sup>[32]</sup> and is shown as black ribbon diagram made in swisspdb viewer software.<sup>[43]</sup> The bound state can arise either due to transient interactions with the core (green lines) or transient tight stacking with the neighboring N-terminal strand (blue lines). In the free state (orange wiggly line) the domain can undergo relatively large scale fluctuations, which are not possible in any of the bound states.



**Figure 8.** Experimental results for the A2-CD<sub>3</sub> site in A $\beta_{1-40}$  fibrils recorded at 37 °C and 14.1 T. A) <sup>2</sup>H static solid-state NMR line shapes for the dry (dotted line) and hydrated (solid line) states.<sup>[17]</sup> B) Experimental (circles) and simulated (lines) Q-CEST profiles.  $I(t)/I(0)$  integrated over the entire spectrum versus  $\Omega/2\pi$  for saturation times of 20 ms (red) and 1 ms (blue) and  $\omega_{RF}/2\pi$  of 1.3 and 2.5 kHz, as indicated on the panels. Simulations were performed according to the model in Figure 7A as described in the text. C) A heat map plot of  $\exp(-20 \cdot \text{RMSD})$  versus  $D$  and  $k_{ex}$  for the experimental Q-CEST profile shown in B) for  $\omega_{RF}/2\pi = 1.3$  kHz,  $t = 20$  ms and simulations performed according to the 2-site exchange model with a single free state and single bound state at a 92%/8% population ratio.

### 2.3.2. M35-CD<sub>3</sub> Site Spanning the Water-Accessible Cavity in the Fibril Core

Earlier work based on line shape and longitudinal relaxation data indicated three main motional modes for the side chain of M35:<sup>[21–22]</sup> rotameric exchange, methyl axis diffusive motions and fast 3-site jumps of the methyl deuterons. In principle, there are 27 possible rotamers of the M35 side chain corresponding to three possibilities for each of the three side chain dihedral angles  $\chi_1$ ,  $\chi_2$  and  $\chi_3$ . To fit the quadrupolar line shapes, it is sufficient to represent this ensemble using four artificial symmetrical conformers with geometry defined by the tetrahedral arrangement (Figure 7B). Further, it is sufficient to represent the populations of these conformers as one major and three equivalent minor conformers in a  $w$ :1:1:1 ratio and a single rotameric inter-conversion constant between each of them,  $k_{\text{ex}}$ . At 37 °C, these parameters correspond to  $w=6$  and  $k_{\text{ex}}=1.0 \cdot 10^5 \text{ s}^{-1}$ . Methyl axis diffusion was modeled as a motion along a restricted arc with a length of 34°. At 37 °C, it had a minor effect on the line shapes but significantly affected longitudinal relaxation. Fast 3-site jumps occur at a timescale much faster than  $C_q$  and, thus, their only effect on the line shape is the averaging of the quadrupolar coupling constant by a factor of one-third.

Thus, the rotameric exchange mode with an effective  $C_q$  value of 58 kHz is expected to make a dominant contribution to the Q-CEST profiles. As for the A2 site, we performed the experiments at the values of  $\omega_{\text{RF}}/2\pi$  of 1.3 and 2.5 kHz with saturation times of 3, 20 and 40 for  $\omega_{\text{RF}}/2\pi=1.3$  kHz and 3 and 20 for  $\omega_{\text{RF}}/2\pi=2.5$  kHz. Unlike the A2-CD<sub>3</sub> Q-CEST line shapes, the M35-CD<sub>3</sub> site Q-CEST line shapes show distortions as a

function of the offset  $\Omega/2\pi$  (Figure 9A), with the most evident distortions in the  $-10$  to  $10$  kHz range. While presenting the Q-CEST experimental and simulated saturation profiles for this site (Figure 9C) we, therefore, integrated over this spectral region.

When the rotameric exchange mode is employed using the parameters that fitted the quadrupolar echo line shape in the previous work (i.e., a 6:1:1:1 population ratio and  $k_{\text{ex}}=1.0 \cdot 10^5 \text{ s}^{-1}$ ), the Q-CEST profiles are much wider than those seen in the experiment (Figure S6A). The smaller angle fluctuations of the methyl axis, which were previously modeled as the diffusion along the restricted arc, cannot narrow these profiles, which are dominated by the large 109.5° angle rotameric exchange. Thus, modeling the experimental Q-CEST profile requires a modification to the approach. In the same model of one major rotamer, the experimental Q-CEST profiles can be matched with a population ratio of 6:1:1:1 and a  $k_{\text{ex}}$  of  $1.5 \cdot 10^6 \text{ s}^{-1}$ . However, these parameters then disagree with the line shape data (Figure S6B). We thus invoke two major rotameric states with equal populations and still a single rotameric exchange constant. The simplest approach is to keep the ratio of the first major conformer to the minor ones unmodified (i.e., the ratio of populations becomes 6:6:1:1). This approach permits us to match both the experimental Q-CEST profiles and the experimental quadrupolar echo line shape (Figures 9B and S6B) with  $k_{\text{ex}}=3.5 \cdot 10^6 \text{ s}^{-1}$ . If two rotameric exchange constants are employed, an even better quality fit could be obtained. However, there is no qualitative improvement and we, therefore, suffice with the single  $k_{\text{ex}}$  rate constant for all the rotameric inter-conversions.

Figure S6C shows the sensitivity of the fits of the Q-CEST profile to the value of  $k_{\text{ex}}$ , indicating that the quality of the fit

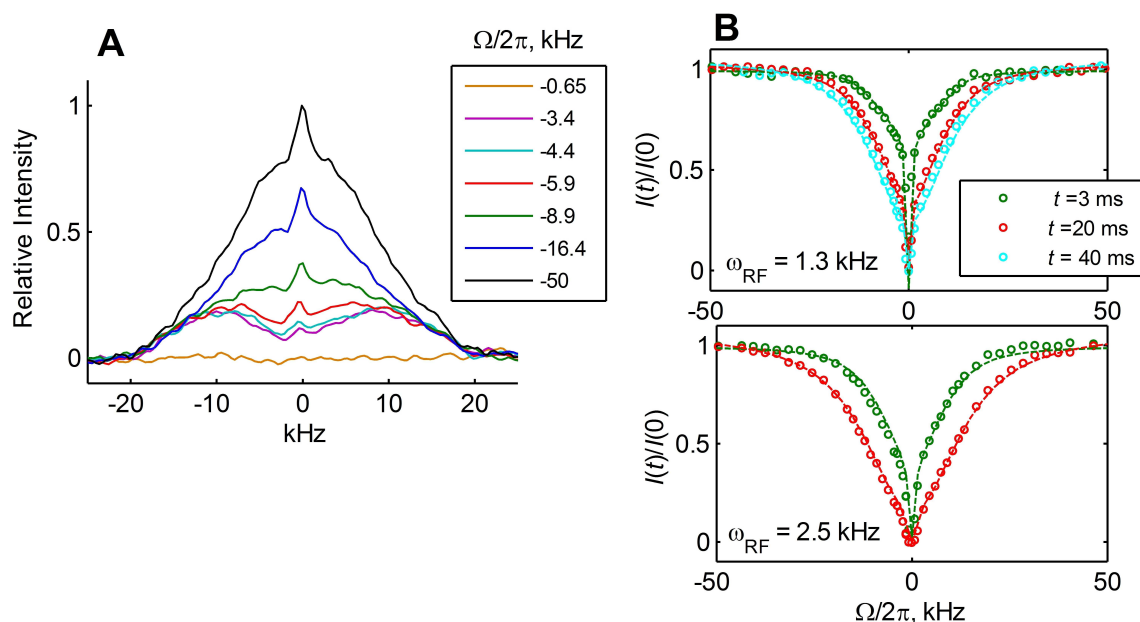


**Figure 9.** Experimental <sup>2</sup>H CEST results for the M35-CD<sub>3</sub> site in Aβ<sub>1–40</sub> fibrils recorded at 37 °C and 14.1 T. A) Examples of the Q-CEST line shapes for different values of  $\Omega/2\pi$  normalized to the intensity at  $\Omega/2\pi = -50$  kHz. B) Experimental (circles) and simulated (lines) Q-CEST profiles  $I(t)/I(0)$  integrated over the  $-10$  to  $10$  kHz spectral region versus  $\Omega/2\pi$  for saturation times of 40 ms (blue) 20 ms (red) and 3 ms (green) and  $\omega_{\text{RF}}/2\pi$  of 1.3 and 2.5 kHz, as indicated on the panels. Simulations were performed according to the rotameric exchange model in Figure 7B with  $w=6$  and  $k_{\text{ex}}=3.5 \cdot 10^6 \text{ s}^{-1}$ .

deteriorates outside the  $3\text{--}4\cdot 10^6\text{ s}^{-1}$  range. We did not explore the dependence of the fits on the values of  $w$  because the interdependence between the  $w$  and  $k_{\text{ex}}$  parameters can only be resolved using additional measurements such as temperature dependence. These measurements were previously performed for the line shape analysis that provided the values of  $w$  used here. Overall, the Q-CEST profiles provided more detailed information on the rotameric inter-conversions of the M35 side chains than the line shape measurements. In particular, Q-CEST suggested the presence of two major rotameric conformers and provided further constraints on the rotameric exchange rate constant.

### 3. Conclusions

The deuterium Q-CEST measurements presented here are useful for a wide range of applications in which the details of the motions on ms- $\mu$ s timescales are important. Spin-1 properties, modest quadrupolar coupling strength and sensitivity to motions yield characteristic saturation profiles that are suitable for motional modeling analysis. A theoretical/computational framework requires the full Liouvillian treatment, as is often the case for solid-state applications. We performed explicit motional modeling in which the rates of motions and populations of states are included in the exchange matrix of Eq. (5). The analysis of the Q-CEST profiles for the individual crystallites of the powder sample for simple 2-site exchange scenarios (Figures 4 and 5) provided insights into the origin of the major features of the profiles and some analogy with the solution NMR coalescence scenarios.

The experiment employed modest saturation fields (1–5 kHz is expected to be sufficient for most applications), which do not damage the sensitive biological samples. Here, we employed static solid-state conditions that require selective site labeling techniques for site-specific information. Extension to magic-angle spinning conditions is possible and will be a subject of future work. The biological applications presented here show that the most accurate results on dynamical ensembles require a range of techniques from simple line shapes to  $R_{1\rho}$  and CPMG-based approaches and CEST measurements.

The results for the  $\text{A}\beta_{1-40}$  fibrils at the A2- $\text{CD}_3$  site are consistent with a previous work employing static  $^2\text{H}$   $R_{1\rho}$  and QCPMG approaches and they expand the view of the dynamical ensemble of the disordered N-terminal region. In particular, the combined analysis of all experiments indicates multiple free states that undergo isotropic diffusion over a range of timescales ( $D$  of  $3\cdot 10^6$  to  $1\cdot 10^8\text{ rad}^2/\text{s}$ ) and participate in a conformational exchange with the bound state, likely arising from transient inter and intra-molecular interactions; the  $k_{\text{ex}}$  of different states spans the values of  $2\cdot 10^4$  to  $3\cdot 10^6\text{ s}^{-1}$ . The M35- $\text{CD}_3$  side chain, pointing inside the water-accessible cavity inside the fibril core of the 3-fold symmetric polymorph, undergoes extensive rotameric exchange. The Q-CEST data permitted us to refine the distribution of the rotameric population and timescale of the rotameric inter-conversions in comparison to the earlier line shape measurements at this site.

Two major and two minor rotamers in a 6:6:1:1 ratio with  $k_{\text{ex}} = 3.5\cdot 10^6\text{ s}^{-1}$  are identified by the Q-CEST measurements, while the line shape data could not differentiate between the scenarios of one or two major rotameric conformers.

## Experimental Section

### Sample Preparation

Samples of  $\text{A}\beta_{1-40}$  in the twisted/3-fold symmetric polymorph were prepared as described in previous work<sup>[17,21]</sup> starting with synthetic peptides, which incorporated selectively labeled amino acids and employed established protocols.<sup>[33,36]</sup> The  $\text{A}\beta_{1-40}$  peptide sequence is DAEFRHDSGYEVHHQKLVFFAEDVGSNKGAIIGLMVGGVV. Two samples were prepared with labels at either the A2- $\text{CD}_3$  or the M35- $\text{CD}_3$  positions. Their morphologies were confirmed by transmission electron microscopy (see Supporting Information for details of the procedures). A hydrated state with a water content of 200% by weight was achieved by exposing lyophilized powder to water vapor in a sealed chamber at 25 °C until the water content reached saturation levels corresponding to about 40% by weight, followed by pipetting the remaining water using deuterium-depleted  $\text{H}_2\text{O}$ . DMS was purchased from Cambridge Isotope Laboratories, Inc. (MA). The samples were packed in 5 mm NMR tubes (cut to 21 mm length), using Teflon tape to center the sample volume in the coil of the NMR probe.

### NMR Spectroscopy for Amyloid Fibril Samples

The experiments were performed on a 14.1 T spectrometer equipped with a Bruker NEO console and a static wide line low-E probe with a 5 mm diameter coil.<sup>[37]</sup> The temperature was set to 37 °C. The pulse sequence of Figure 1 was used with RF fields of 1.3 and 2.5 kHz, off-resonance offsets between  $-50$  and  $50$  kHz and saturation times in the range of 1–40 ms. The RF field strength calibrations were performed as described in previous work utilizing the spin-lock-based method of the transverse component<sup>[31]</sup> and employing a  $\text{D}_2\text{O}$  sample due to a weak RF field, which cannot lock wide powder patterns. The quadrupolar echo  $\tau$  delay was set to 31  $\mu\text{s}$  and hard  $90^\circ$  pulse length was 2.0  $\mu\text{s}$ . In total, 32 dummy scans were used. The number of scans ranged from 256 to 1024, with a larger number used for offsets close to the zero frequency. The inter-scan delay was set to 0.7–1.5 s. Spectra were processed with a 1 kHz exponential line broadening function.

### Simulations

Evolution under Q-CEST: The simulations followed the elements of the pulse sequence outlined in Figure 1. The evolution of spin coherence during the saturation period was obtained by the direct exponentiation of the Liouville–von Neumann matrix of Eqs. (5) and (6) using the internal Matlab function.<sup>[38]</sup> The relaxation terms due to rapidly oscillating quadrupole interactions were calculated separately in the Redfield limit according to the conformational exchange model appropriate for each case and the resulting relaxation rates were equal for all exchanging sites. The evolution during the saturation period was calculated in the doubly-rotating frame, with the additional rotation occurring around the z-axis of the laboratory frame with a frequency equal to the offset  $\Omega$ . Backward rotation was applied to the coherence obtained at the end of the evolution period to return it to the singly-rotating frame. The details of the motional modeling of the matrices  $K$  entering Eq. (5) is specified below for each of the special cases considered.

The detection block involving the quadrupolar echo scheme (with idealized 90° pulses), the powder averaging procedure involving appropriate Euler's angle transformations and the set-up of motional frames were taken from the EXPRESS program.<sup>[39]</sup>

2-site exchange: The exchange between the two sites with selected relative orientations (0 or 109.5° for theoretical calculations, 106° for DMS) was set up with forward and reverse rate constants in ratios necessary to obtain the predetermined equilibrium populations for each site.

A2-CD<sub>3</sub>: The exchange matrix  $K_{ij}$  combines the components responsible for the isotropic diffusion and conformational exchange between the free diffusion state and bound state, according to the following scheme:

$$K = \left( \begin{array}{c|c} \text{diffusion} & \text{exchange} \\ \hline \text{exchange with bound state} & \text{with bound state} \\ \hline & \text{state} \end{array} \right)$$

The block of the exchange matrix  $K_{ij}$  responsible for the diffusion is represented by nearest-neighbor jumps with sites of equal populations distributed (almost) uniformly on the surface of the sphere and with identical exchange rates between the sites,  $K_{ij} = k_D$ . We used the program DistMesh,<sup>[40]</sup> which creates a uniform distribution of sites by assuming a linear repulsive force and solving for the equilibrium. The inclusion of  $N_D = 192$  sites is sufficient to adequately represent the isotropic diffusion process. Due to the spin 1 symmetry properties, only the second-order spatial spherical harmonics give rise to the spectral densities. Thus, the second-order eigenfunction of the Smoluchowski diffusion equation encodes the spatial reorientation and the corresponding eigenvalue is related to the diffusion coefficient  $D$  as  $D(l+1) = 6D$ . As expected, the simulated eigenvalues of  $K_{ij}$  appear in groups of  $2l+1$ , corresponding to the eigenvectors with the angular momentum  $l$  of the continuous limit of the diffusion equation. The five eigenvalues  $\lambda_2$  corresponding to  $l = 2$  are then averaged to obtain the numerical value of  $D$ . This establishes the correspondence between  $D$  and  $k_D$  as  $k_D = 6D/\langle\lambda_2\rangle$ .<sup>[17]</sup> The exchange was modeled by jumps between every site describing the spherical diffusion and bound-state site. The relative weights of each site were expressed through the ratio of the forward and reverse rate constants for the exchange process. Modeling the exchange with two free states and one bound state (Figure 6A) included two sets of 192 sites describing the surface of a sphere with the corresponding nearest-neighbor jump constants within each set as well as independent exchange constants between every site of each of the two sets and an arbitrarily fixed site in the crystal-fixed frame corresponding to the bound state.

M35-CD<sub>3</sub>: Rotameric jumps were modeled as occurring between four symmetrical conformers pointing toward the corners of the tetrahedron, following computational approaches developed previously.<sup>[41–42]</sup> Two main scenarios of populations and rates were considered: a) one major and three minor conformers with populations in a  $w:1:1:1$  ratio and an identical conformational exchange jump rate  $k_{ex}$  for all conformers; and b) two major and two minor conformers with populations in a  $w:w:1:1$  ratio and an identical conformational exchange jump rate  $k_{ex}$  for all conformers (Figure 6B). The supporting Information of reference<sup>[41]</sup> provides the Euler angles necessary to define the geometry of these motions.

The tensor parameters for A2 and M35 were taken as  $C_q = 55.5$  (A2) and  $C_q = 58$  kHz (M35),  $\eta = 0$ ; these represent averaging over fast methyl jumps.<sup>[22,42]</sup> Longitudinal relaxation was taken into account phenomenologically (with  $T_1 = 50$  ms for A2 and  $T_1 = 300$  ms for M35) by including an additional term in the Liouvillian evolution matrix, which was identical for all eight coherences of Eq. (6). This approach was tested for DMS for which the inclusion of the 3-site jumps mode explicitly yielded the same results.

## Acknowledgments

This work was supported by a National Institutes of Health Grant 1R15-GM111681. Experiments were performed at the National High Magnetic Field Laboratory, which is supported by NSF Cooperative Agreement NSF/DMR-1644779, the State of Florida and the U.S. Department of Energy. Some of the measurements utilized a 9.4 T spectrometer at CU Denver supported by NSF grant 1726947.

- [1] A. G. Palmer 3rd, *J. Magn. Reson.* **2014**, *241*, 3–17.
- [2] P. Vallurupalli, G. Bouvignies, L. E. Kay, *J. Am. Chem. Soc.* **2012**, *134*, 8148–8161.
- [3] G. Bouvignies, L. E. Kay, *J. Phys. Chem. B* **2012**, *116*, 14311–14317.
- [4] A. G. Palmer, H. Koss, in *Methods in Enzymology*, Vol. 615 (Ed.: A. J. Wand), Academic Press, **2019**, pp. 177–236.
- [5] N. L. Fawzi, J. Ying, R. Ghirlando, D. A. Torchia, G. M. Clore, *Nature* **2011**, *480*, 268–272.
- [6] H. M. McConnell, *J. Chem. Phys.* **1958**, *28*, 430–431.
- [7] A. Abragam, *Principles of Nuclear Magnetism*, Clarendon Press, Oxford, **1961**.
- [8] P. Schanda, M. Ernst, *Prog. Nucl. Magn. Reson. Spectrosc.* **2016**, *96*, 1–46.
- [9] P. Rovó, R. Linsler, *J. Phys. Chem. B* **2017**, *121*, 6117–6130.
- [10] A. B. Siemer, K. Y. Huang, A. E. McDermott, *Proc. Natl. Acad. Sci. USA* **2010**, *107*, 17580–17585.
- [11] M. S. Greenfield, A. D. Ronemus, R. L. Vold, R. R. Vold, P. D. Ellis, T. E. Raidy, *J. Magn. Reson.* **1987**, *72*, 89–107.
- [12] C. Grey, W. S. Veeman, A. J. Vega, *J. Chem. Phys.* **1993**, *98*, 7711–7724.
- [13] A. J. Vega, *J. Magn. Reson.* **1992**, *96*, 50–68.
- [14] S. Odedra, S. Wimperis, *Solid State Nucl. Magn. Reson.* **2017**, *84*, 4–13.
- [15] R. R. Vold, in *Nuclear Magnetic Resonance Probes of Molecular Dynamics* (Ed.: R. Tycko), Kluwer academic Publishers, Dordrecht, **1994**, pp. 27–112.
- [16] L. Vugmeyster, D. F. Au, D. Ostrovsky, R. Fu, *ChemPhysChem* **2019**, *20*, 1680.
- [17] D. F. Au, D. Ostrovsky, R. Fu, L. Vugmeyster, *J. Biol. Chem.* **2019**, *294*, 5840–5853.
- [18] T. Wang, H. Jo, W. F. DeGrado, M. Hong, *J. Am. Chem. Soc.* **2017**.
- [19] Y. Miller, B. Ma, R. Nussinov, *J. Am. Chem. Soc.* **2011**, *133*, 2742–2748.
- [20] M. McDonald, H. Box, W. Bian, A. Kendall, R. Tycko, G. Stubbs, *J. Mol. Biol.* **2012**, *423*, 454–461.
- [21] L. Vugmeyster, M. A. Clark, B. I. Falconer, D. Ostrovsky, D. Gantz, W. Qiang, G. L. Hoatson, *J. Biol. Chem.* **2016**, *291*, 18484–18495.
- [22] L. Vugmeyster, D. Ostrovsky, M. A. Clark, B. I. Falconer, G. L. Hoatson, W. Qiang, *Biophys. J.* **2016**, *111*, 2135–2148.
- [23] J. R. C. van der Maarel, *J. Chem. Phys.* **1993**, *99*, 5646–5653.
- [24] S. E. Ashbrook, S. Wimperis, *J. Chem. Phys.* **2004**, *120*, 2719–2731.
- [25] A. G. Palmer, C. D. Kroenke, J. P. Loria, *Methods Enzymol.* **2001**, *339*, 204–238.
- [26] M. J. Brown, R. L. Vold, G. L. Hoatson, *Solid State Nucl. Magn. Reson.* **1996**, *6*, 167–185.
- [27] C. M. Quinn, A. E. McDermott, *J. Biomol. NMR* **2012**, *222*, 1–7.
- [28] V. V. Gerardy-Montouillout, C. Malveau, P. Tekely, Z. Olender, Z. Luz, *J. Magn. Reson. Ser. A* **1996**, *123*, 7–15.
- [29] D. E. Favre, D. J. Schaefer, B. F. Chmelka, *J. Magn. Reson. A* **1998**, *134*, 261–279.
- [30] L. Frydman, S. Vallabhaneni, Y. K. Lee, L. Emsley, *J. Chem. Phys.* **1994**, *101*, 111–117.
- [31] L. Vugmeyster, D. Ostrovsky, *ChemPhysChem* **2019**, *20*, 333–342.

- [32] A. K. Paravastu, I. Qahwash, R. D. Leapman, S. C. Meredith, R. Tycko, *Proc. Natl. Aca. Sci. U. S. A.* **2009**, *106*, 7443–7448.
- [33] A. T. Petkova, R. D. Leapman, Z. H. Guo, W. M. Yau, M. P. Mattson, R. Tycko, *Science* **2005**, *307*, 262–265.
- [34] A. K. Paravastu, R. D. Leapman, W. M. Yau, R. Tycko, *Proc. Natl. Aca. Sci. U. S. A.* **2008**, *105*, 18349–18354.
- [35] R. L. Vold, R. R. Vold, in *Advances in Magnetic and Optical Resonance, Vol. 16* (Ed.: W. Warren), Academic Press, San Diego, **1991**, pp. 85–171.
- [36] A. T. Petkova, W. M. Yau, R. Tycko, *Biochemistry* **2006**, *45*, 498–512.
- [37] P. L. Gor'kov, E. Y. Chekmenev, C. Li, M. Cotten, J. J. Buffy, N. J. Traaseth, G. Veglia, W. W. Brey, *J. Magn. Reson.* **2007**, *185*, 77–93.
- [38] N. J. Higham, *SIAM J. Matrix Anal. Appl.* **2005**, *26*, 1179–1193.
- [39] R. L. Vold, G. L. Hoatson, *J. Magn. Reson.* **2009**, *198*, 57–72.
- [40] P.-O. Persson, G. Strang, *SIAM Rev.* **2004**, *46*, 329–345.
- [41] L. Vugmeyster, D. Ostrovsky, A. Khadjinova, J. Elden, G. L. Hoatson, R. L. Vold, *Biochemistry* **2011**, *50*, 10637–10646.
- [42] L. Vugmeyster, D. Ostrovsky, J. J. Ford, S. D. Burton, A. S. Lipton, G. L. Hoatson, R. L. Vold, *J. Am. Chem. Soc.* **2009**, *131*, 13651–13658.
- [43] N. Guex, M. C. Peitsch, *Electrophoresis* **1997**, *18*, 2714–2723.

---

Manuscript received: November 3, 2019  
 Revised manuscript received: November 30, 2019  
 Accepted manuscript online: December 5, 2019  
 Version of record online: January 9, 2020